4-10-2019

Formability of a HSAS Based on Hot Processing Maps and Texture Analyses

Zhiqiang Yang
Yanshan University, China

Ligang Liu
Yanshan University, China

Tongguang Zhai
University of Kentucky, tongguang.zhai@uky.edu

Chunmei Zhao
Yanshan University, China

Hui Yu
Yanshan University, China

See next page for additional authors

Formability of a HSAS Based on Hot Processing Maps and Texture Analyses

Digital Object Identifier (DOI)
https://doi.org/10.1088/2053-1591/ab14ab

Notes/Citation Information

Published in *Materials Research Express*, v. 6, no. 7, 076538, p. 1-11.

Authors

Zhiqiang Yang, Ligang Liu, Tongguang Zhai, Chunmei Zhao, Hui Yu, and Qiang Li

Formability of a HSAS based on hot processing maps and texture analyses

Materials Research Express

PAPER

Formability of a HSAS based on hot processing maps and texture analyses

Zhiqiang Yang[1], **Ligang Liu**[1,3], **Tongguang Zhai**[2], **Chunmei Zhao**[1], **Hui Yu**[1] and **Qiang Li**[1,3]

[1] College of Mechanical Engineering, Yanshan University, Qinhuangdao, People's Republic of China
[2] Department of Chemical and Materials Engineering, University of Kentucky, Lexington, United States of America
[3] Authors to whom any correspondence should be addressed.

E-mail: lgliu@ysu.edu.cn **and** liqiang@hebut.edu.cn

Keywords: high strength steel, processing map, instability criterion, texture, deformation

OPEN ACCESS

RECEIVED
27 January 2019

REVISED
7 March 2019

ACCEPTED FOR PUBLICATION
29 March 2019

PUBLISHED
10 April 2019

Abstract

Aiming to improve the formability of a HSAS Docol 1500 Bor, hot processing maps were obtained based on Prasad, Babu and Murty instability criteria. The hot processing maps based on the above instability criteria are similar and the explanation of its similarity is given. Recrystallization and misorientation in typical quenched specimens were observed by using SEM with a EBSD system. It was found that the fraction values of HAGBs in quenched martensite are all below 0.4 under experimental conditions. Flow location bands occurs at lower deformation temperatures and higher strain rates. The textures in martensite mainly include ⟨110⟩//ND and ⟨110⟩//RD components. Based on N-W OR, the textures in deformed austenite are mostly ⟨111⟩//ND and ⟨112⟩//RD⟩ components. Prasad and Babu instability criteria are more conservative than Murty instability criterion in obtaining the processing maps of the tested steel. To reduce the anisotropy of quenched workpieces because of the textures at room temperature, the quenching temperature in the stamping process of the tested steel should be lower.

1. Introduction

The high strength automobile steels (HSAS) with high yield strength and high tensile strength have been widely used in production of automobile stamping parts. To improve the formability of HSAS, many studies have been carried out on the composition [1], mechanical properties [2], processing technologies etc [3, 4]. The processing map is an effective and popular tool to study the deformation behaviors of a wide range of materials such as steels [5], aluminum alloys [6] and Ni-based superalloys [7]. By using processing map, the instability regimes can be predicted and the optimized process parameters can be obtained [8, 9].

Many researchers have proposed some stability and instability criteria of materials [10, 11]. Gegel and Malas constructed similar stability criteria by using Lyapunov functional stability criterion [12, 13]. Prasad [14], Babu [15], Murty and Rao [16] had developed different instability criteria based on the maximum principle of irreversible thermodynamics applied to large plastic rheology. Some typical research works had been carried out to compare the prediction accuracy of these stability or instability criteria [17–20]. Li *et al* constructed the processing and instability maps of titanium alloy Ti-6.5Al-3.5Mo-1.5Zr-0.3Si based on the Prasad, Murty and Malas criteria. Li *et al* found that the predicted results based on the Murty and Prasad criteria were not much different, which were quite different from the results predicted by the Malas criterion [17]. Wang *et al* proved that the Gegel and Alexander-Malas stability criteria were mathematically equivalent and thus predicted the same unstable region in ultrahigh strength stainless steels [18]. Zhou *et al* compared the processing maps of superalloy GH4742 with different instability criteria of Prasad, Gegel, Malas, Murty and Semiatin. The results show that Murty instability criterion was most suitable for superalloy GH4742 [19].

For the high strength automobile steel (HSAS) products, the microstructure obtained is homogeneous quenched martensite after hot stamping and quenching processes. The microstructure characteristics of

quenched martensite affect the performance of workpieces to a large extent, which inherit from austenite at high temperatures [21, 22].

In this work, the hot deformation behaviours of a HSAS are studied by using the processing maps constructed based on different criteria at isothermal compression conditions. Furtherly, the influence of deformation conditions on textures in the quenched microstructure are discussed theoretically by using scanning electronic microscope (SEM) Canta650 with a EBSD system. The aim is to analyse the relationship between the textures of quenched martensite and the deformation conditions at high temperatures.

2. Experimental procedure

2.1. Material and hot compression test

The chemical compositions of the tested HSAS Docol 1500 Bor are 0.22%C-0.2%Cr-1.15%Mn-0.3%Si-0.003%B-0.03%P-0.01%S in weight percentage. To dissolve the precipitates such as carbides and obtain a homogenous microstructure, the tested steel was solution annealed. The solution temperature was 1120 °C and the solution time is 3 h. The cylindrical specimen with dimensions of ϕ8 mm×15 mm from the homogenized piece were isothermally compressed on a thermal-mechanical simulator Gleeble-3800. The specimens were heated to 1050 °C and held for 5 min to ensure the uniformity of temperatures then cooled with cooling rate of 10 °C/s to the test temperatures of 900, 950, 1000 and 1050 °C and held for 3 min followed by compression tests at the engineering strain of 0.2, 0.4 and 0.6, respectively, while the strain rates ranged from 0.01to 10 s^{-1}. Tantalum sheets were stuck on the both end faces of cylindrical specimens to reduce friction. The specimens were immediately quenched in water after compression tests.

2.2. Microstructure observation

The room temperature microstructures after deformation at 900 °C and strain rates of 0.01–10 s^{-1}were carefully examined on an optical microscope. The quenched specimens were sliced along the longitudinal direction, then prepared by mechanical polishing and revealed by using 4 wt% Nital etching for 9 s.

Microstructure evolution in instability and stability domains was observed by using SEM with a EBSD system. Then some typical deformed specimens were selected and sliced along the longitudinal direction for EBSD examination, which were carefully prepared first by mechanical polishing and followed by electro-polishing in a perchloric acid solution (8 vol% $HClO_4$, 90 vol% C_2H_5OH and 2 vol% $C_3H_8O_3$) at 17 V for 20 s. The EBSD analysis was performed by S-4800 field emission scanning electron microscopy coupled with a fully automated with a TSL-OIM™ EBSD attachment, operated at 25 kV. For the compressed specimens in this work, scans were performed over an area of 250 μm × 50 μm with a step size of 0.3–1.5 μm depending on the grain size.

3. Experimental results

3.1. Flow Stresses during deformation and the deformed microstructures

Figure 1 shows the flow stress curves of the tested steels during compression tests at different temperatures and strain rates. The critical stress σ_c, critical strain ε_c, peak stress σ_p and peak strain ε_p was shown in figure 1. The critical strain was the valley value of the $d\theta/d\sigma-\sigma$ curves, where θ was the work hardening rate, $\theta = (\partial\sigma/\partial\varepsilon)_{\dot{\varepsilon}}$ [23, 24]. It can be seen from figure 1 that the flow tresses decrease with increasing deformation temperatures or decreasing strain rates. At higher temperatures such as 1000 and 1050 °C, the flow stress curves show obvious peaks at all experimental strain rates, which indicate that continue dynamic recrystallization (DRX) occurs during hot compression. In contract, at lower temperatures such as 900 and 950 °C, the most of the flow stress curves are nearly flat, which shows the typical characteristic of dynamic recovery (DRV) during hot deformation.

Figure 2 show the strain hardening rate-true stress curves at 950 °C and strains of 0.01, 0.1, 1 and 10 s^{-1}. The strain hardening rate will taper off to zero when no DRX occurs. The presence of DRX causes a downward inflection in the strain hardening rate-true stress curves, leading to zero and negative strain hardening rates, which corresponds to peak and post peak softening, respectively. In this work, the stress peaks can be precisely measured as 58.2, 79.3 and103.3 MPa for HSAS Docol 1500 Bor steel at strain rates of 0.01,0.1,1 and 10 s^{-1}, respectively.

Figure 3 shows the transformed martensite after at 950 °C and strain rates of 0.01, 0.1, 1 and 10 s^{-1} when the strain is 0.6. It can be seen from figure 3 that a large amount of lath martensite exits in the deformed specimens. The morphology of quenched martensite grains reflects that the deformed grain size decreases with increasing strain rates. At the strain rates of 1 and 10 s^{-1}, the finer martensite grain results from the deformed austinite at high temperatures, where DRV is the major phenomena as shown in figures 3(c) and (d). Because martensitic transformation occurs after deformation, the deformation streamline at high temperatures could not be seen

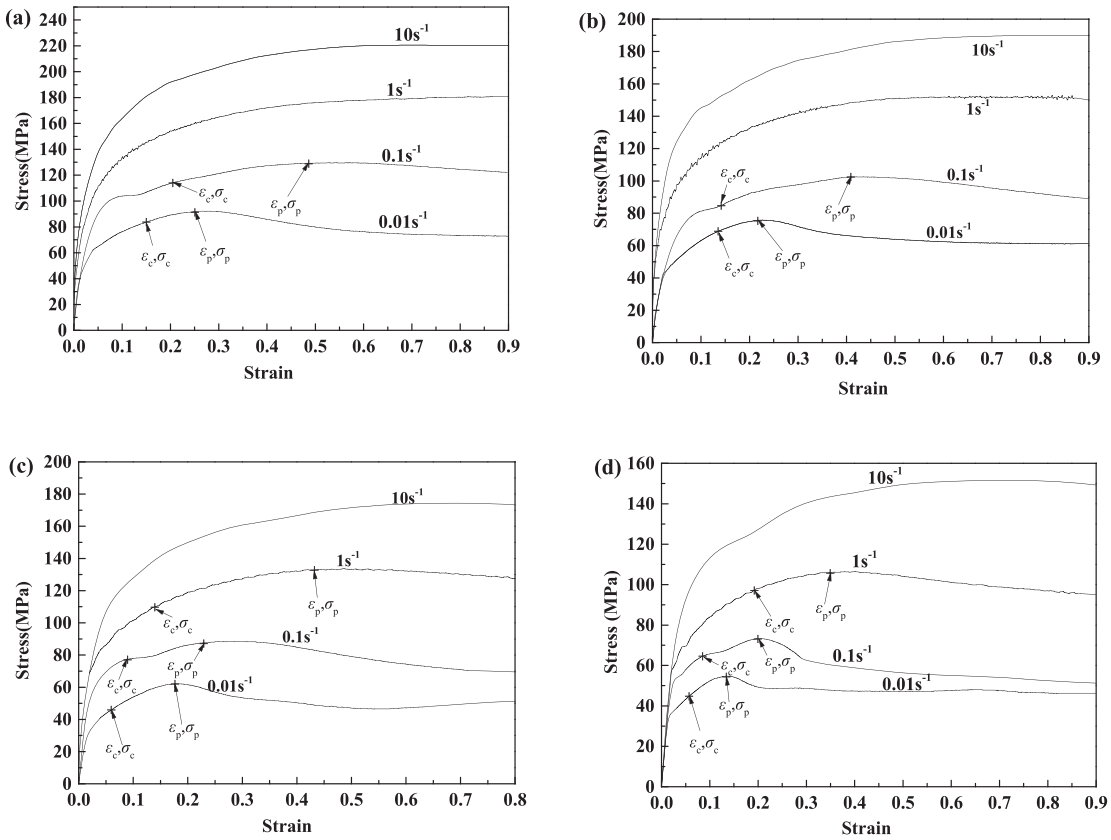

Figure 1. True stress-strain curves of Steel Docol 1500 Bor during hot compression: (a) 900 °C, (b) 950 °C, (c) 1000 °C, (d) 1050 °C.

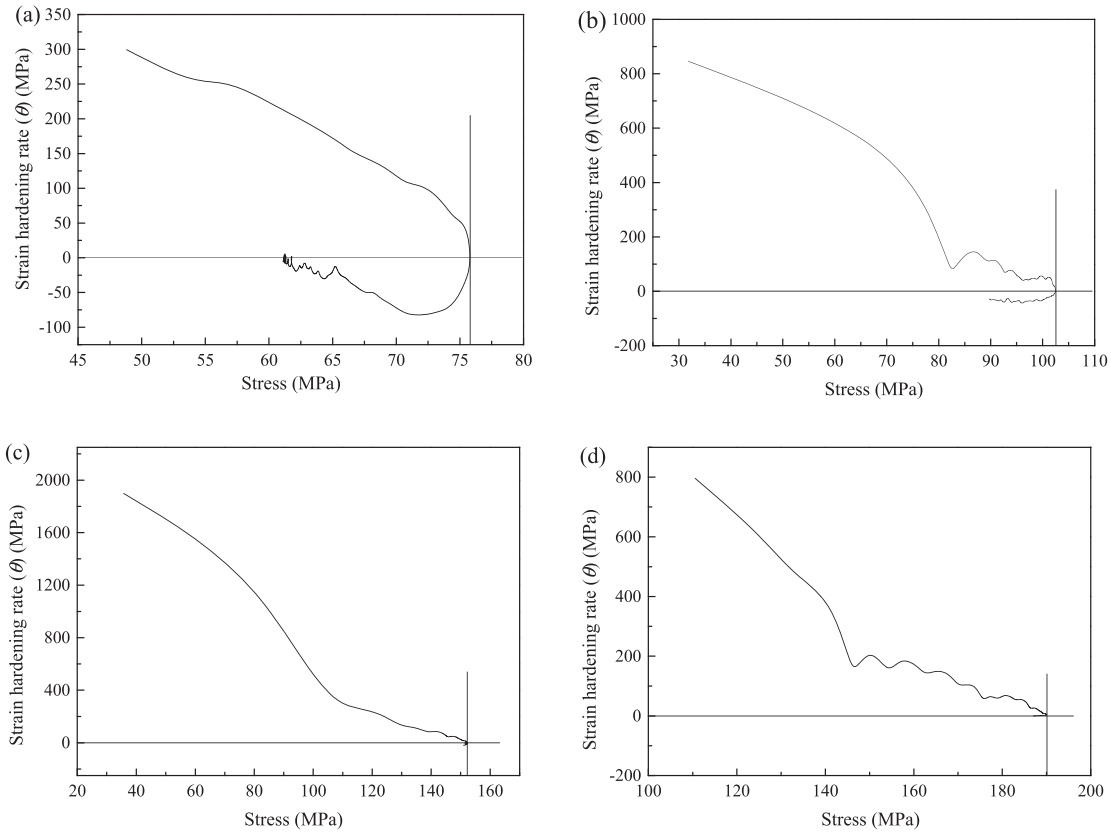

Figure 2. Strain hardening rate versus true stress at 950 and strains of 0.001, 0.01 and 0.1s-1for the tested steel.

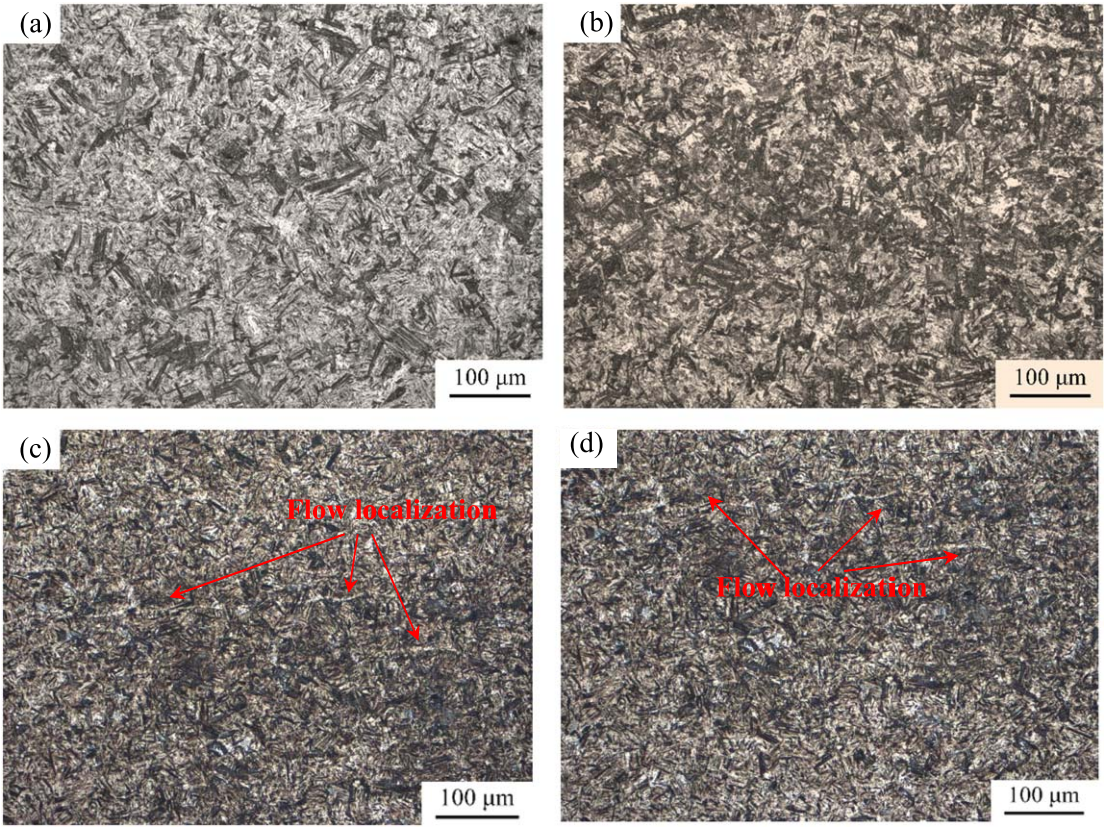

Figure 3. Microstructures of specimens deformed at 950 °C and different strain rates: (a) 0.01 s^{-1}, (b) 0.1 s^{-1}, (c) 1 s^{-1}, (d) 10 s^{-1}.

clearly. However, the local deformation bands can also be observed in figures 3(c) and (d), which indicates the occurrence of flow localization.

3.2. Processing maps

At present, the processing map has become a very powerful approach to optimize the hot working processes and further control the microstructures and properties of the metal products. Basing on the dynamic materials model (DMM), The total power P absorbed by the work piece is the sum of two complementary functions:

$$P = \sigma \cdot \dot{\varepsilon} = G + J = \int_0^{\dot{\varepsilon}} \sigma d\dot{\varepsilon} + \int_0^{\sigma} \dot{\varepsilon} d\sigma \tag{1}$$

where G, J, σ and $\dot{\varepsilon}$ represent the power dissipations in the form of a temperature rising, the one caused by microstructure evolution such as DRX, DRV and phase transition, the flow stress and the strain rate, respectively.

The strain rate sensitivity, m describes the power portioning between G and J, which can be expressed as follows:

$$m = \frac{dJ}{dG} = \frac{d(ln\sigma)}{d(ln\dot{\varepsilon})} \approx \frac{\Delta ln\sigma}{\Delta ln\dot{\varepsilon}} \tag{2}$$

The efficiency of power dissipation, η presents the power dissipated through microstructure changes during hot deformation, which could be derived as a function of strain rate sensitivity:

$$\eta = \frac{J}{J_{max}} = \frac{2m}{m+1} \tag{3}$$

where J_{max} is the theoretically maximum value of J. Then the power dissipation map plotting the efficiency of power dissipation η against temperatures and strain rates can be obtained, in which different domains with various η values present the diverse microstructural mechanism. It is generally accepted that the domains with high efficiency are considered as the optimum deformation conditions. However, for the instances that instable plastic deformation or flow localization occur, the efficiency of power dissipation alone is not sufficient to identify the unsafe domains. Fortunately, this problem has been overcame in virtue of instability criterion $\xi_P(\dot{\varepsilon}, T)$ for plastic flow proposed by Ziegler [25].

$$\xi_P(\dot{\varepsilon},\ T) = \frac{\partial ln\left(\frac{m}{m+1}\right)}{\partial ln\dot{\varepsilon}} + m < 0 \tag{4}$$

Equation (4) is deduced by the assumption that the flow stress-strain rate curve follows a power-law relation $\sigma = K\dot{\varepsilon}^m$, in which m is constant. However, m varies with $\dot{\varepsilon}$ in reality. Murty and Rao proposed an instability criterion applicable for any type of stress-strain rate curves [16].

$$\xi_M(\dot{\varepsilon},\ T) = \frac{2m}{\eta_M} - 1 < 0 \tag{5}$$

where η_M is the efficiency of power dissipation in instability criterion $\xi_M(\dot{\varepsilon}, T)$, which should be deduced by its original definition.

$$\eta_M = \frac{J}{J_{\max}} = \frac{J}{P/2} = \frac{2(P-G)}{P} = 2\left[1 - \frac{1}{\sigma\dot{\varepsilon}}\int_0^{\dot{\varepsilon}} \sigma d\dot{\varepsilon}\right] \tag{6}$$

It is assumed that the flow stress-strain rate curve between 0 and $\dot{\varepsilon}_{\min}$ follows the constitutive equation $\sigma = K\dot{\varepsilon}^m$, the value of m between 0 and $\dot{\varepsilon}_{\min}$ can be replaced by the gradient of lnε-ln$\dot{\varepsilon}$ curve at the strain rate of $\dot{\varepsilon}_{\min}$. Then the equation (6) can be modified as follows:

$$\eta_M = 2\left[1 - \frac{1}{\sigma\dot{\varepsilon}}\left(\left(\frac{\sigma\dot{\varepsilon}}{m+1}\right)_{\dot{\varepsilon}=\dot{\varepsilon}_{\min}} + \int_{\dot{\varepsilon}_{\min}}^{\dot{\varepsilon}} \sigma d\dot{\varepsilon}\right)\right] \tag{7}$$

Babu *et al* deduced another instability criterion based on the one proposed by Murty, which was also applicable for any type of stress-strain rate curves.

$$\xi_B(\dot{\varepsilon},\ T) = \frac{\partial m}{\partial ln\dot{\varepsilon}} + m^2 < 0 \tag{8}$$

Figures 4, 5 and 6 are the processing maps at different engineering strain based on the instability criteria $\xi_P(\dot{\varepsilon}, T)$, $\xi_B(\dot{\varepsilon}, T)$ and $\xi_M(\dot{\varepsilon}, T)$, respectively. The processing maps based on the instability criteria $\xi_P(\dot{\varepsilon}, T)$ and $\xi_B(\dot{\varepsilon}, T)$ are very similar at each strain. At the engineering strain of 0.2, unstable regions exit in the regions with high temperatures and high stain rates as shown in figures 4(a) and 5(a). The unstable regions move to the regions with low temperatures and high strain rates, which become larger with increasing strain as shown in figures 4(b), (c), 5(b) and (c). No unstable region exits in the processing maps based on the instability criterion $\xi_M(\dot{\varepsilon}, T)$ at the engineering strain of 0.2 as shown in figure 6(a). The processing maps based on the instability criterion $\xi_B(\dot{\varepsilon}, T)$ at the large engineering strain show the same rule with those built based on the instability criteria $\xi_P(\dot{\varepsilon}, T)$ and $\xi_B(\dot{\varepsilon}, T)$, of which the unstable regions are slightly smaller than those built based on the instability criteria $\xi_P(\dot{\varepsilon}, T)$ and $\xi_B(\dot{\varepsilon}, T)$ as shown in figures 6(b) and (c). The distribution rules of η values in the processing maps built based on instability criterion $\xi_M(\dot{\varepsilon}, T)$ are roughly the same as those based on instability criteria $\xi_P(\dot{\varepsilon}, T)$ and $\xi_B(\dot{\varepsilon}, T)$, while the maximum η values are present in different deformation conditions as shown in figures 4, 5 and 6.

Equation (5) can be modified as follows:

$$\xi_M(\dot{\varepsilon},\ T) = 2m - \frac{2J}{P} < 0 \tag{9}$$

Take partial differentiation of $\dot{\varepsilon}$ on both sides of equation (9):

$$\frac{\partial m}{\partial\dot{\varepsilon}}\sigma\dot{\varepsilon} + m\frac{\partial\sigma}{\partial\dot{\varepsilon}}\dot{\varepsilon} + m\sigma - \frac{\partial J}{\partial\dot{\varepsilon}} < 0 \tag{10}$$

The differential form of the formula $J = \int_\sigma^0 \dot{\varepsilon}\mathrm{d}\sigma$ are shown as follows:

$$J = \dot{\varepsilon}\mathrm{d}\sigma = \dot{\varepsilon}\frac{d\partial}{d\dot{\varepsilon}}d\dot{\varepsilon} = \frac{\dot{\varepsilon}}{\sigma}\frac{d\partial}{d\dot{\varepsilon}}\sigma d\dot{\varepsilon} = m\sigma d\dot{\varepsilon} \tag{11}$$

Then,

$$\frac{\partial m}{\partial\dot{\varepsilon}}\sigma\dot{\varepsilon} + m\frac{\partial\sigma}{\partial\dot{\varepsilon}} < 0 \Rightarrow \frac{\partial m}{\partial\ \ln\dot{\varepsilon}}\sigma + m\frac{\partial\sigma}{\partial\ \ln\dot{\varepsilon}} < 0 \tag{12}$$

Both sides of the equation (12) are divided by σ, then the instability criterion $\xi_B(\dot{\varepsilon}, T)$can be obtained as same as equation (8).

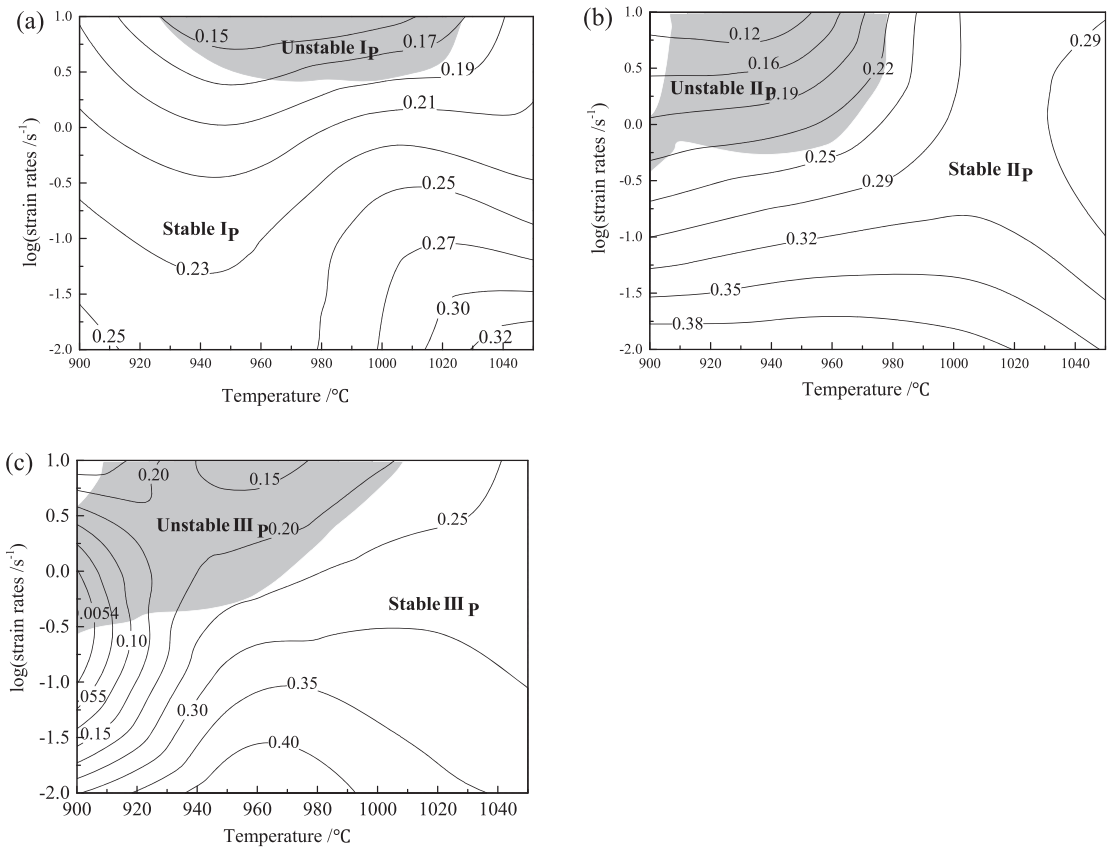

Figure 4. Processing maps for Steel Docol 1500 Bor generated at engineering strains of: (a) 0.2, (b) 0.4, and (c) 0.6 based on the instability criterion $\xi_P(\dot{\varepsilon},\ T)$.

The instability criterion $\xi_p\ (\dot{\varepsilon}, T)$ can be expressed as follows:

$$\xi_P(\dot{\varepsilon},\ T) = \frac{\partial \ln\left(\frac{m}{m+1}\right)}{\partial\left(\frac{m}{m+1}\right)} \frac{\partial\left(\frac{m}{m+1}\right)}{\partial m} \frac{\partial m}{\partial \ln \dot{\varepsilon}} + m < 0 \tag{13}$$

Then,

$$\xi_P(\dot{\varepsilon},\ T) = \frac{m+1}{m} \frac{1}{(m+1)^2} \frac{\partial m}{\partial \ln \dot{\varepsilon}} + m < 0 \tag{14}$$

$$\xi_P(\dot{\varepsilon},\ T) = \frac{1}{m(m+1)} \frac{\partial m}{\partial \ln \dot{\varepsilon}} + m < 0 \tag{15}$$

Because:

$$G < P \Rightarrow 1 < \frac{\dot{\varepsilon}}{\sigma} \frac{\partial \sigma}{\partial \dot{\varepsilon}} + 1 \Rightarrow 1 < m + 1 \Rightarrow m > 0 \tag{16}$$

and:

$$J < G \Rightarrow \frac{dJ}{dG} \leqslant 1 \Rightarrow m \leqslant 1 \tag{17}$$

It can be known from equations (16) and (17) that $0 < m < 1$.Therefore, the instability criterion $\xi_p\ (\dot{\varepsilon}, T)$ can be modified as follows:

$$\xi_P(\dot{\varepsilon},\ T) = \frac{\partial m}{\partial \ln \dot{\varepsilon}} + m^2 + m^3 < 0 \tag{18}$$

It can be found that an extra m^3 exits in the instability criterion $\xi_p\ (\dot{\varepsilon}, T)$ by comparing equations (8) and (18). Because $0 < m < 1$, m^3 has little influence on the calculation results of equation (18). Then it can be known that the instability criterion $\xi_p\ (\dot{\varepsilon}, T)$, $\xi_B\ (\dot{\varepsilon}, T)$ and $\xi_M(\dot{\varepsilon}, T)$ are the same in theory, which can be used to explain the similarity reflected in figures 4, 5 and 6.

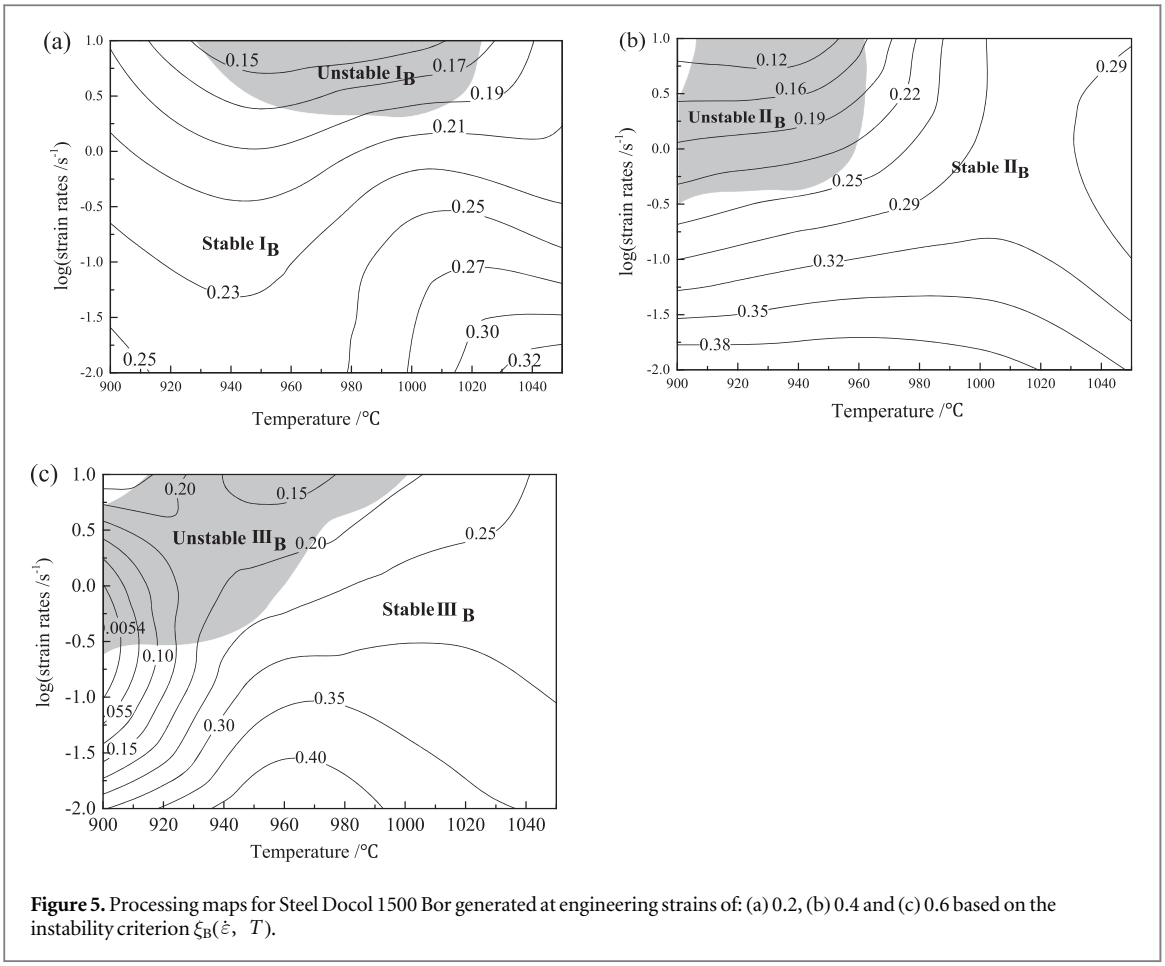

Figure 5. Processing maps for Steel Docol 1500 Bor generated at engineering strains of: (a) 0.2, (b) 0.4 and (c) 0.6 based on the instability criterion $\xi_B(\dot{\varepsilon}, T)$.

3.3. Recrystallization and texture analysis

Martensitic transformation is non-diffusive phase transformation. The size of austenite at high temperatures determine the size of quenched martensite. Then, the size of quenched martensite can be used to study the degree of recrystallization of deformed austenite. In this work, the grain tolerance angle of 1° was used to determine whether two neighbouring scan points belong to the same grain. Figure 7 shows the misorientation angle distributions of quenched martensite grains under different deformation conditions.

It can be seen that the fraction of high angle grain boundaries (HAGBs)(15°–180°) of martensite increase with increasing the deformation temperatures and deceasing strain rates of parent austenite at the same strain as shown in figure 7. At the engineering strain of 0.2, the fraction values of HAGBs of martensite at the deformation temperature of 1050 °C and strain rates of 1 and 10 s^{-1} are 0.286 and 0.268, respectively, while those at the strain rate of 1 s^{-1} and temperatures of 950 and 1050 °C are 0.286 and 0.31, respectively. The same change law exists at the engineering strain of 0.6 as shown in figures 7(e)–(h). At the same time, the fraction of HAGBs of martensite increases with increasing strain at the same temperatures and strain rates as shown in figures 7(d) and (h), which increases from 0.299 to 0.366 at the deformation temperature of 1050 °C and strain rates of 10 s^{-1} when engineering strain increases from 0.2 to 0.6. The increasing of the fraction of HAGBs of martensite means that more recrystallization has completed in deformed parent austenite at high temperatures. However, referring to figure 1, no complete dynamic recrystallization occurs at temperatures of 950, 1050 °C and strain rates of 1, 10 s^{-1}, respectively, when the strain was 0.2, which leads to the low fraction of HAGBs as shown in figures 7(a)–(d).

The experimental orientation relationship (OR) between plate martensite and prior austenite is close to the Nishiyama–Wassermann (N-W) OR ($\{111\}_\gamma \| \{110\}_\alpha$, $\langle 112\rangle_\gamma \| \langle 110\rangle_\alpha$). These textures in lath martensite influence the plasticity at low temperatures, causing different deformation behavior along different directions of the sheet workpieces. For correlating anisotropic properties of the HSAS products with textures, it is necessary to describe the textures in a quantitative way. To achieve the statistical purpose, in several uniform deformation region was selected and the quenched martensite textures under specific deformation conditions was measured by using TSL OIM analysis software, of which the typical grain distribution was shown in figure 8.

From figure 8, it can be seen that the textures in the quenched martensite in this work mainly include $\langle 110\rangle$//ND ($\{110\}\langle 001\rangle$, $\{110\}\langle -110\rangle$, $\{110\}\langle -112\rangle$ and $\{110\}\langle 1\text{–}12\rangle$), $\langle 110\rangle$//RD ($\{001\}\langle 110\rangle$, $\{110\}$

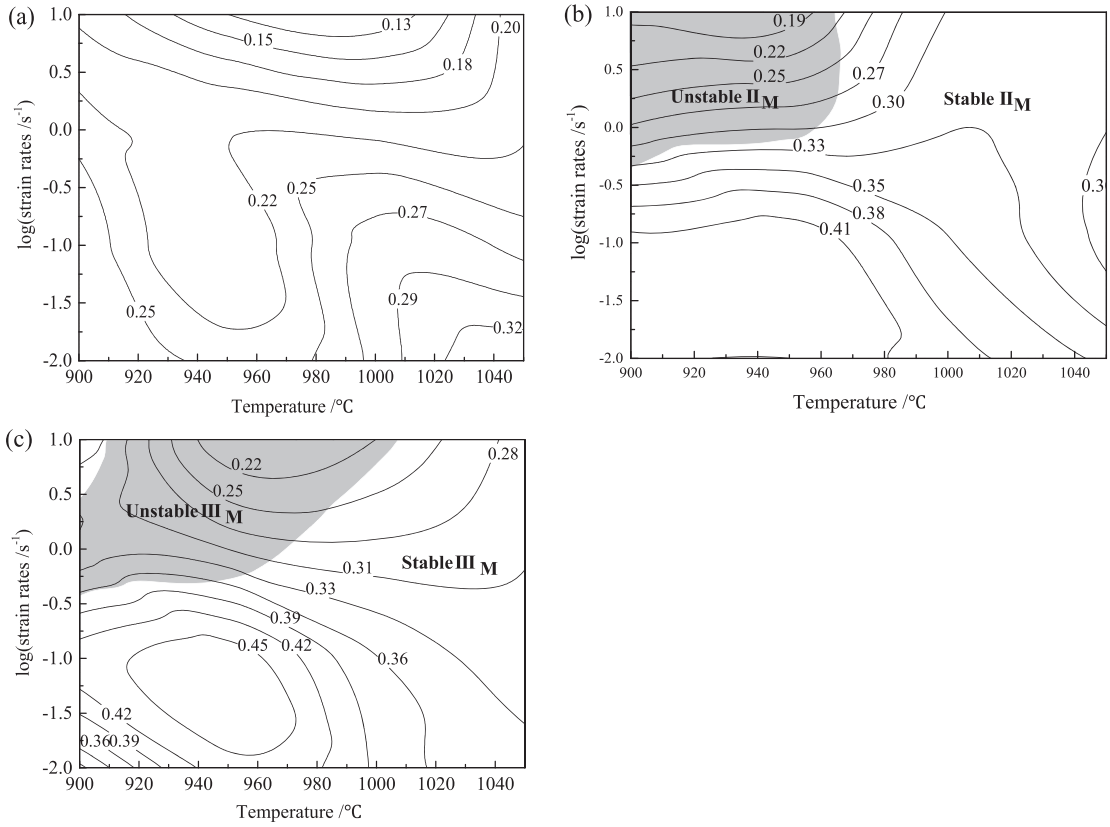

Figure 6. Processing maps for Steel Docol 1500 Bor generated at engineering strains of: (a) 0.2, (b) 0.4 and (c) 0.6 based on the instability criterion $\xi_M(\dot{\varepsilon}, T)$.

⟨1–10⟩, {110}⟨−110⟩, {112}⟨−110⟩ and {112}⟨1–10⟩) and relatively fewer ⟨001⟩//ND ({001}⟨100⟩ and {001}⟨110⟩), of which the former two components belong to ζ fiber and α fiber, respectively. The measured OR of the quenched martensite in this work is closed to the N–W OR.

At the engineering strain of 0.2 as shown in figures 8(a), (b), (c) and (d), The measured orientation has no obvious preferred orientation and no texture exit in quenched martensite, which should result from no preferred orientation appears in deformed austenite at high temperatures because of the low strain. Meanwhile, the fraction values of recrystallization at the strain rates of 1 and 10 s^{-1} at the temperature of 950 °C have no significant difference, while the same situation exits at the temperature of 1050 °C as shown in figures 7(c) and (d). Therefore, the deformation is easy to occur at the engineering strain of 0.2 and the presences of the Unstable zones I_P and I_B in figures 4(a) and 5(a) are not reasonable, which agrees with literature [17]. Then the processing maps based on the instability criterion $\xi_M(\dot{\varepsilon}, T)$ are more reasonable compared with the two ones based on the instability criteria $\xi_P(\dot{\varepsilon}, T)$ and $\xi_B(\dot{\varepsilon}, T)$ as shown in figures 4(a), 5(a) and 6(a).

For figures 8(e), (f), (g) and (h) at the engineering strain of 0.6, the distributions of textures show obvious preferred orientation. The quenched martensite texture mainly includes ⟨110⟩//ND and ⟨110⟩//RD components, which correspond to the ⟨111⟩//ND and ⟨112⟩//RD texture components in recrystallization austenite after compression deformation at high temperatures. In generally, recrystallization of compression-deformed steel tends to retain the deformation texture component [111]//ND [26]. Then the recrystallization austenite has the similar texture characteristics with the deformed austenite. For figures 8(f) and (g), the fraction of quenched martensite texture components ⟨110⟩//ND is less, from which we can deduce that less deformed austenite texture components ⟨111⟩//ND appears. Then the deformability of tested steels was deteriorated, which verify the correctness of the processing maps in this work. At room temperature, the fraction of martensite texture component ⟨110⟩//ND increased with increasing deformation temperatures and decreasing deformation rates, which has the same variation rule with the austenite dynamic recrystallization at high temperature. Then the ⟨111⟩//ND texture mainly results from recrystallized austenite. The content of the textures in quenched martensite is lower at the deformation temperature of 900 °C, which is beneficial to reduce the anisotropy of workpieces. Therefore, the quenching temperature in the stamping process of the tested steel can be lower, for example, 900 °C.

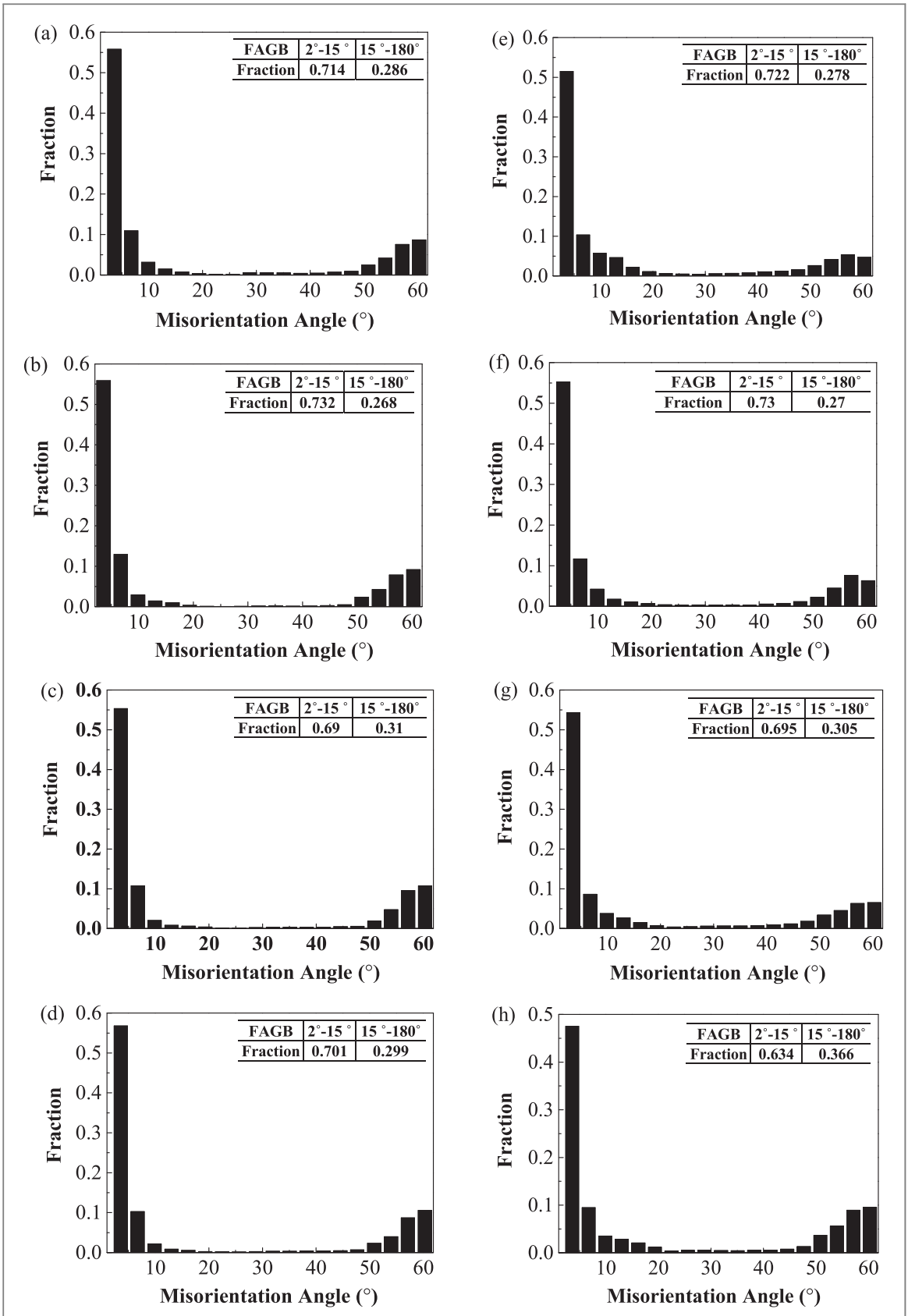

Figure 7. Misorientation distributions for the grain boundaries under different deformation conditions: (a) $\varepsilon = 0.2$, $T = 950$ °C, $\dot{\varepsilon} = 1$ s^{-1}; (b) $\varepsilon = 0.2$, $T = 950$ °C, $\dot{\varepsilon} = 10$ s^{-1}; (c) $\varepsilon = 0.2$, $T = 1050$ °C, $\dot{\varepsilon} = 1$ s^{-1}; (d) $\varepsilon = 0.2$, $T = 1050$ °C, $\dot{\varepsilon}$=10 s^{-1}; (e) $\varepsilon = 0.6$, $T = 900$ °C, $\dot{\varepsilon} = 0.1$ s^{-1}; (f) $\varepsilon = 0.6$, $T = 900$ °C, $\dot{\varepsilon} = 1$ s^{-1}; (g) $\varepsilon = 0.6$, $T = 1000$ °C, $\dot{\varepsilon} = 10$ s^{-1}; (h) $\varepsilon = 0.6$, $T = 1050$ °C, $\dot{\varepsilon} = 10$ s^{-1}.

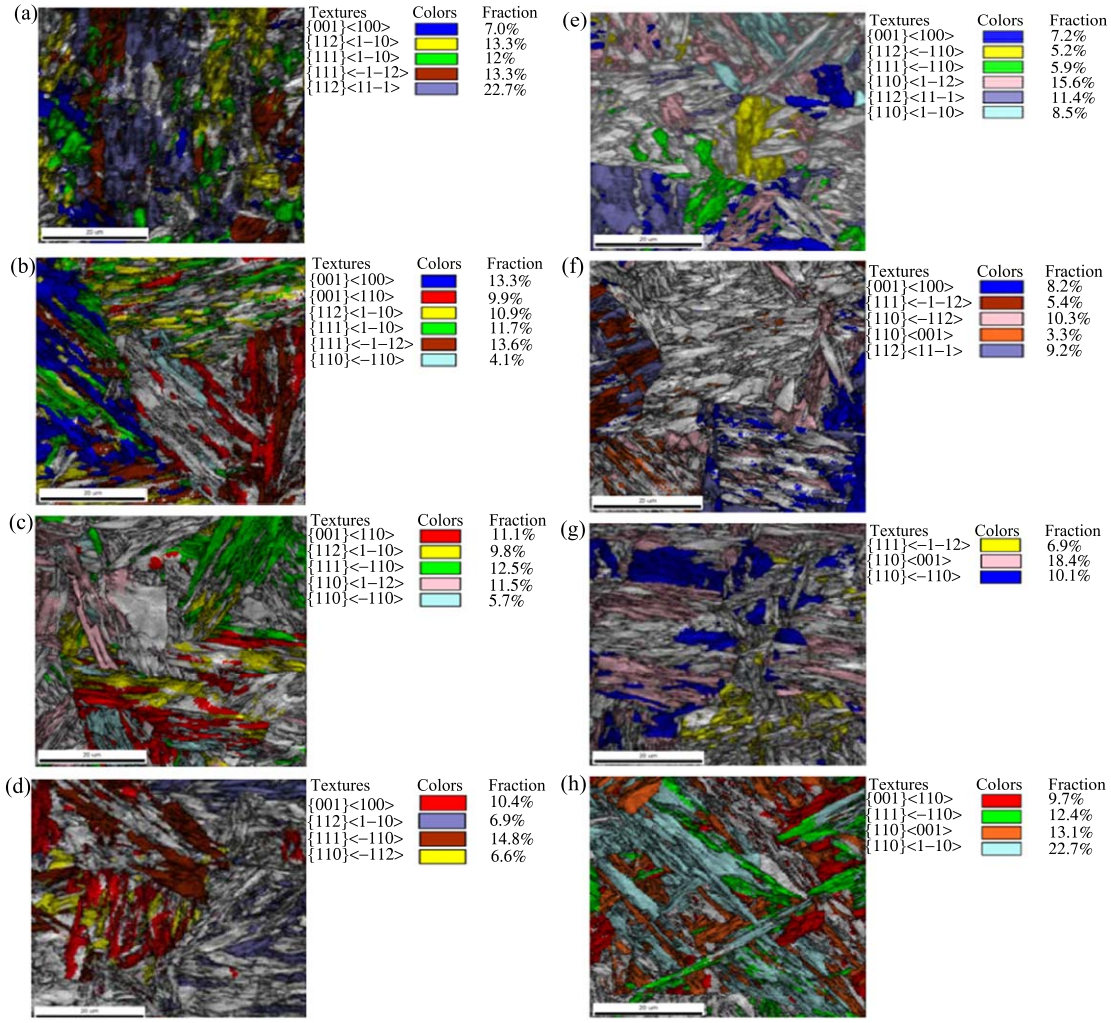

Figure 8. Grain size distribution in specific orientations under different deformation conditions: (a) $\varepsilon = 0.2$, $T = 950$ °C, $\dot{\varepsilon} = 1$ s^{-1}; (b) $\varepsilon = 0.2$, $T = 950$ °C, $\dot{\varepsilon} = 10$ s^{-1}; (c) $\varepsilon = 0.2$, $T = 1050$ °C, $\dot{\varepsilon} = 1$ s^{-1}; (d) $\varepsilon = 0.2$, $T = 1050$ °C, $\dot{\varepsilon} = 10$ s^{-1}; (e) $\varepsilon = 0.6$, $T = 900$ °C, $\dot{\varepsilon} = 0.1$ s^{-1}; (f) $\varepsilon = 0.6$, $T = 900$ °C, $\dot{\varepsilon} = 1$ s^{-1}; (g) $\varepsilon = 0.6$, $T = 1000$ °C, $\dot{\varepsilon} = 10$ s^{-1}; (h) $\varepsilon = 0.6$, $T = 1050$ °C, $\dot{\varepsilon} = 10$ s^{-1}.

4. Conclusion

The following conclusions can be drawn from this work:

(1) The processing maps adopting the instability criteria $\xi_P(\dot{\varepsilon}, T)$ and $\xi_B(\dot{\varepsilon}, T)$ are relatively more conservative compared with that using the instability criterion $\xi_M(\dot{\varepsilon}, T)$, which are more reliable.

(2) HAGBs in quenched martensite increase with increasing deformation temperatures and deceasing strain rates of deformed austenite at the same strain, which also increase with increasing strain. In this work, the fraction values of HAGBs in quenched martensite are all less than 0.4 under all deformation conditions.

(3) For steel Docol 1500 Bor, no texture appears in quenched martensite at the engineering strain of 0.2. The deformed austenite texture mainly include ⟨111⟩//ND and ⟨112⟩//RD⟩ components at the engineering strain of 0.6. The recrystallization texture component ⟨111⟩//ND in deformed austenite decreases with decreasing the deformation temperatures and increasing the strain rates. The flow location bands, the decrease of DRX and texture component ⟨111⟩//ND deteriorates the deformability of tested steels.

(4) Generally, the texture in quenched martensite mainly includes ⟨110⟩//ND and ⟨110⟩//RD components. The content of textures in quenched martensite is lower at the deformation temperature of 900 °C. To reduce the anisotropy of quenched workpieces, the quenching temperature in the stamping process of the tested steel should be lower.

Acknowledgments

The authors are grateful for the financial support from the Major Scientific and Technological Specialities of High-grade CNC Machine Tools and Basic Manufacturing Equipment (No. 2018ZX04023002), National

Natural Science Foundation of China (No. 51205342) and Natural Science Foundation of Hebei Province of China (No. E2016203217).

ORCID iDs

Ligang Liu https://orcid.org/0000-0001-8778-8598

References

[1] Huang H, Yang G, Zhao G, Mao X, Gan X, Yin Q and Yi H 2018 Effect of Nb on the microstructure and properties of Ti-Mo microalloyed high-strength ferritic steel *Mat. Sci. Eng.* A **736** 148–55
[2] Li Y, Song R, Jiang L and Zhao Z 2019 Strength response of 1200 MPa grade martensite-ferrite dual-phase steel under high strain rates *Scripta Mater.* **164** 21–4
[3] Dai Z, Ding R, Yang Z, Zhang C and Chen H 2018 Thermo-kinetic design of retained austenite in advanced high strength steels *Acta Mater.* **152** 288–99
[4] Zhou Y, Song X, Liang J, Shen Y and Misra R D K 2018 Innovative processing of obtaining nanostructured bainite with high strength-high ductility combination in low-carbon-medium-Mn steel: process-structure-property relationship *Mat. Sci. Eng.* A **718** 267–76
[5] Yang Z, Zhang F, Zheng C, Zhang M, Lv B and Qu L 2015 Study on hot deformation behaviour and processing maps of low carbon bainitic steel *Mater. Design* **66** 258–66
[6] Suresh K, Dharmendra C, Rao K P, Prasad Y V R K and Gupta M 2015 Processing Map of AZ31-1Ca-1.5 vol% Nano-Alumina composite for hot working *Mater. Manuf. Process.* **30** 1161–7
[7] Zhang P, Hu C, Ding C, Zhu Q and Qin H 2015 Plastic deformation behavior and processing maps of a Ni-based superalloy *Mater. Design* **65** 575–84
[8] Quan G, Zhang L, Wang X and Li Y 2017 Correspondence between microstructural evolution mechanisms and hot processing parameters for Ti-13Nb-13Zr biomedical alloy incomprehensive processing maps *J. Alloy. and Comp.* **698** 178–93
[9] Son H W, Jung T K, Lee J W and Hyun S K 2017 Hot deformation characteristics of CaO-added AZ31 based on kinetic models and processing maps *Mat. Sci. Eng.* A **695** 379–85
[10] Springer P and Prahl U 2016 Characterisation of mechanical behavior of 18CrNiMo7-6 steel with and without nb under warm forging conditions through processing maps analysis *J. Mater. Process. Tech.* **237** 216–34
[11] Bombac D, Brojan M, Tercelj M and Turk R 2009 Response to Hot Deformation Conditions and Microstructure Development of Nimonic 80A Superalloy *Mater. Manuf. Process.* **24** 644–8
[12] Gegel H L *et al* 1987 *Metals Handbook* 9th edn (Metals Park: Ohio: ASM International)
[13] Malas J 1991 Methodology for design and control of thermomechanical processes *PhD Dissertation* Ohio University, Athens, OH
[14] Prasad Y V R K 1990 Recent advances in the science of mechanical processing *Indian J. Technol.* **28** 435–51
[15] Babu N S, Tiwari S B and Rao B N 2013 Modified instability condition for identification of unstable metal flow regions in processing maps of magnesium alloys *Mater. Sci. and Tech.* **21** 976–84
[16] Murty S V S N and Rao B N 1999 Instability map for hot working of 6061 Al-10 vol% metal matrix composite *J. Phys. D: Appl. Phys.* **31** 3306–11
[17] Li X, Lu S, Wang K, Fu M W and Cao C 2013 Analysis and comparison of the instability regimes in the processing maps generated using different instability criteria for Ti–6.5Al–3.5Mo–1.5Zr–0.3Si alloy *Mat. Sci. Eng.* A **576** 259–66
[18] Wang X, Liu Z and Luo H 2017 Hot deformation characterization of ultrahigh strength stainless steel through processing maps generated using different instability criteria *Mater. Charact.* **131** 480–91
[19] Zhou G, Ding H and Cao F 2014 A Comparative study of various flow instability criteria in processing map of superalloy GH4742 *J. Mater. Sci. Technol.* **30** 217–22
[20] Zhang J, Di H and Mao K 2013 Processing maps for hot deformation of a high-Mn TWIP steel: a comparative study of various criteria based on dynamic materials model *Mat. Sci. Eng.* A **587** 110–22
[21] Miyamoto G, Iwata N, Takayama N and Furuhara T 2010 Mapping the parent austenite orientation reconstructed from the orientation of martensite by EBSD and its application to quenched martensite *Acta Mater.* **58** 6393
[22] Li Z *et al* 2016 Texture inheritance from austenite to 7 M martensite in Ni–Mn-Gamelt-spun ribbons *Results Phys.* **6** 428–33
[23] Mejía I, Bedolla-Jacuinde A, Maldonado C and Cabrera J M 2011 Determination of the critical conditions for the initiation of dynamic recrystallization in boron microalloyed steels *Mat. Sci. Eng.* A **528** 4133–40
[24] Kumar S, Aashranth B, Samantaray D, Davinci M A, Borah U and Bhaduri A K 2018 Influence of nitrogen on kinetics of dynamic recrystallization in Fe-Cr-Ni-Mo steel *Vacuum* **156** 20–9
[25] Ziegler H 1963 *Progress in Solid Mechanics* (New York: Wiley)
[26] Hu H 1974 *Texture of Metals Texture* **1** 233–58